

Article

Bridging deep segmentation and metaverse visualization: Cellpose-based 3D brain tumor reconstruction from MRI

Pranshu Saxena^{1*}, Aatif Jamshed², Sandeep Saxena³, Sanjay Kumar Singh⁴, Sahil Kumar Aggarwal⁵

CITATION

Saxena P, Jamshed A, Saxena S, et al. Bridging deep segmentation and metaverse visualization: Cellpose-b ased 3D brain tumor reconstruction from MRI. Metaverse. 2025; 6(3): 3727. https://doi.org/10.54517/m3727

ARTICLE INFO

Received: 15 May 2025 Accepted: 19 August 2025

Available online: 30 September 2025

COPYRIGHT



Copyright © 2025 by author(s). *Metaverse* is published by Asia Pacific Academy of Science Pte. Ltd. This work is licensed under the Creative Commons Attribution (CC BY) license. https://creativecommons.org/licenses/by/4.0/

Abstract: Accurate and efficient brain tumor segmentation is critical for diagnosis, treatment planning, and outcome monitoring in neuro-oncology. This study presents an integrated framework that combines deep learning-based tumor segmentation with 3D spatial reconstruction and metaverse-aligned visualization. The Cellpose segmentation model, known for its shape-aware adaptability, was applied to grayscale T1-weighted MRI slices to generate binary tumor masks. These 2D masks were reconstructed into 3D surface meshes using the marching cubes algorithm, enabling the computation of clinically relevant spatial parameters including centroid, surface area, bounding box dimensions, and mesh extents. The resulting tumor models were embedded into a global coordinate system and visualized across orthogonal planes, simulating extended reality (XR) environments for immersive anatomical exploration. Quantitative evaluation using DICE, Intersection over Union (IoU), and Positive Predictive Value (PPV) validated the segmentation accuracy, with DICE scores exceeding 0.85 in selected cases. The reconstructed tumors exhibited surface areas ranging from ~45,000 to ~74,000 voxel² units and extended across more than 200 units along the Y and Z axes. Although volumetric values were not computed due to open mesh geometry, the spatial profiles provided a reliable foundation for integration into metaverse platforms. This pipeline offers a lightweight and scalable approach for bridging conventional 2D tumor imaging with immersive 3D applications, paving the way for advanced diagnostic, educational, and surgical planning tools.

Keywords: brain tumor segmentation; cellpose; MRI; 3D reconstruction; marching cubes; metaverse visualization; tumor mesh; medical image analysis

1. Introduction

Brain tumors remain one of the most fatal forms of cancer, contributing to over 250,000 deaths annually worldwide [1, 2]. According to the American Brain Tumor Association, nearly 700,000 people in the United States are currently living with a primary brain tumor, and approximately 85% of all primary central nervous system (CNS) tumors are located in the brain [2]. The clinical workflow for diagnosis heavily relies on Magnetic Resonance Imaging (MRI), which provides excellent soft tissue contrast and non-invasive anatomical detail. However, manually delineating tumors from MRI slices is labor-intensive, highly subjective, and varies significantly among radiologistsTo address this, automated tumor segmentation using deep learning has become a promising solution. Traditional models like U-Net [3], Attention U-Net

¹ School of Computer Science Engineering and Technology, Bennett University, Greater Noida, India.

² Department of Computer Science, KIET Group of Institutions, Delhi-NCR, Ghaziabad, India.

³ School of Computer Science and Engineering, IILM University, Greater Noida, India.

⁴University School of Automation and Robotics, Guru Gobind Singh Indraprastha University, East Delhi Campus, Surajmal Vihar, Delhi 110092, India.

⁵ Department of Information Technology, ABES Engineering College, Ghaziabad, India.

^{*}Corresponding author: Pranshu Saxena, pranshusaxena@gmail.com

[4], and V-Net [5] have shown strong performance in segmenting biomedical images, especially in the context of the BraTS (Brain Tumor Segmentation) challenge. However, these models often require extensive retraining and fine-tuning. Recent advancements have focused on more context-aware and efficient models for medical image segmentation. For instance, NestedFormer [6] proposed a transformer-based architecture for brain tumor segmentation that leverages nested encoder-decoder pathways to better integrate modality-aware features. Segmamba [7] introduced long-range sequential modeling using Mamba, achieving promising results in 3D medical imaging tasks through efficient state-space representations. In parallel, Serp-Mamba [8] advanced retinal vessel segmentation using a selective memory mechanism to balance global and local information, while TP-DRSeg [9] employed explicit text prompts with SAM (Segment Anything Model) to guide lesion segmentation in diabetic retinopathy. These studies exemplify the increasing trend toward integrating transformers, prompts, and state-space models for improved segmentation accuracy, generalizability, and interpretability [10].

Cellpose [6], a generalist deep learning model originally designed for cellular segmentation, has demonstrated adaptability in segmenting irregular and organic shapes using vector flow representations. This makes it particularly useful for medical images, including grayscale MRI slices with high variability in tumor shape and size [9, 10, 11, 12, 13, 14].

Beyond segmentation, converting 2D tumor masks into 3D volumetric models enhances spatial understanding and opens the door for advanced analysis and visualization. The marching cubes algorithm [7, 15] remains the most popular method for reconstructing 3D surface meshes from volumetric data, enabling not only surface visualization but also the extraction of spatial metrics such as surface area, centroid, and extents. These metrics are particularly valuable in neurosurgical planning and volumetric tumor assessment [16, 17].

Recently, the metaverse—an interconnected digital space combining VR [18], AR, and XR—has found applications in healthcare, including medical training, remote diagnostics, and interactive 3D anatomical exploration [8, 18, 19]. In this context, embedding 3D tumor models into spatial coordinate systems allows for intuitive, immersive exploration of pathology. Prior studies have highlighted the effectiveness of XR environments in improving spatial orientation during complex medical tasks [19, 20, 21, 22].

This paper presents a complete pipeline for segmenting brain tumors using Cellpose, reconstructing them into 3D surface models, and integrating them into a coordinate-aware metaverse-style visualization framework. Key spatial parameters such as volume, centroid, bounding box, and surface area are extracted, and the final models are embedded on X, Y, and Z axes to simulate immersive navigation and analysis. The core objectives of this study are:

- To apply Cellpose segmentation to grayscale MRI slices for robust tumor mask prediction.
- To reconstruct 2D tumor masks into realistic 3D surface meshes using marching cubes.
- To extract critical metaverse-aligned spatial parameters such as centroid, bounding box, and surface area.
- To embed 3D tumor models into a 3D coordinate visualization system compatible with XR/VR platforms.

This paper is structured as follows. Section 2 outlines the methodology, including

dataset characteristics, the Cellpose segmentation strategy, and 3D reconstruction techniques. Section 3 presents the implementation and evaluation metrics used. Section 4 explains mesh generation, spatial parameter extraction, and projection into the 3D coordinate system. Section 5 discusses the experimental results, visual outcomes, and parameter interpretations. Section 6 offers a detailed discussion on the significance of the approach, its integration into metaverse frameworks, and current limitations. Section 7 concludes the study, followed by Section 8 which highlights potential directions for future research.

2. Proposed Methodology

The proposed methodology presents a modular and reproducible pipeline designed to automate brain tumor segmentation from 2D MRI slices and transform the output into interactive 3D models suitable for metaverse-aligned environments.

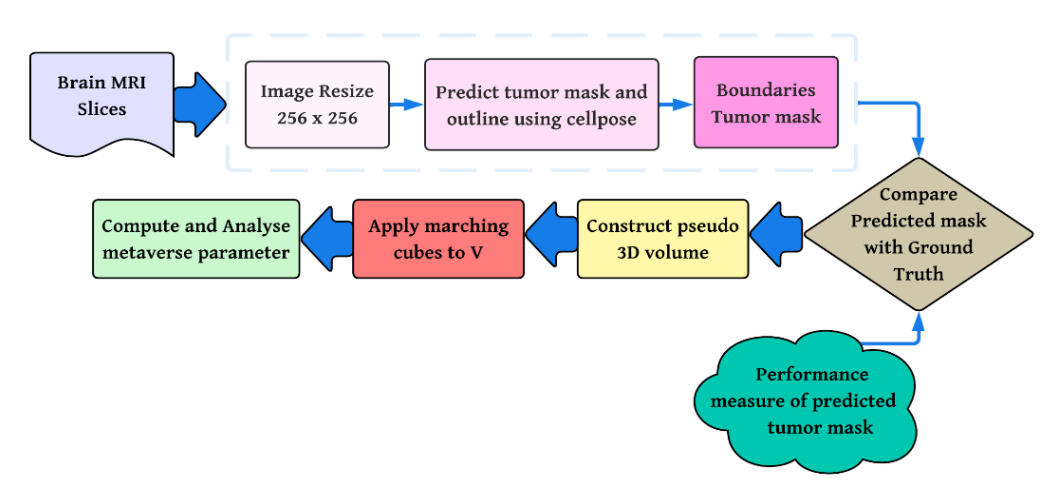


Figure 1. Pipeline for Tumor Segmentation and Metaverse-Aligned 3D Reconstruction from Brain MRI Slices

The framework in **Figure 1** is initiated with tumor segmentation using the Cellpose model, chosen for its generalist vector flow-based architecture that enables accurate delineation of complex and irregular tumor boundaries in grayscale MRI. Following segmentation, the binary masks are volumetrically extruded and reconstructed into surface meshes using the marching cubes algorithm. Key spatial parameters—such as centroid, bounding box, and surface area—are then computed from the generated mesh. These 3D representations are embedded in a coordinate-aware space and projected across orthogonal planes to simulate immersive exploration.

Algorithm 1. Workflow of proposed algorithm

Input:

 $I = \text{Set of grayscale MRI images } \{I_1, I_2, ..., I_n\}$ $M_{GT} = \text{Set of ground truth binary masks } \{M_1, M_2, ..., M_n\}$

Output:

P =Predicted mask set $\{P_1, P_2, ..., P_n\}$

 $O = \text{Outline set } \{O_1, O_2, ..., O_n\}$

V = 3D volume constructed from predictions

Meta = Metaverse parameters (centroid, volume, orientation, bounding box)

Begin:

Cellpose Model ← Load pretrained 'cyto' model

```
P \leftarrow \emptyset, O \leftarrow \emptyset, V \leftarrow \emptyset
   depth ← number of slices to extrude in 3D
For each MRI image I_i \in I do:
     Step 1: Resize I_i to 256 \times 256 \rightarrow I_{resized}
     Step 2: Predict tumor mask and outline using Cellpose:
     [P_i, O_i] \leftarrow Cellpose\ Model\ (I\ resized, channels = [0,0], diameter = None)
     Step 3: Append P<sub>i</sub> to predicted mask set P
     Append Oi to outline set O
     Step 4: Compare P_i with M_i \in M_{GT}
     Compute: DICE, IoU, PPV
End For
Step 5: Construct pseudo-3D volume
Select predicted mask P_k
For z = 1 to depth do
     V[z] \leftarrow P_k
End For
Step 6: Apply marching cubes to V
[verts, faces] \leftarrow marching cubes(V, level = 1)
Step 7: Compute metaverse parameters
Centroid ← mean position of foreground voxels in V
Bounding Box \leftarrow min/max (x, y, z) in V
Orientation \leftarrow [0, 0, 1] (extrusion axis)
Return:
P, O, V, {Centroid, Volume, Bounding Box, Orientation}
```

To ensure algorithmic clarity and reproducibility, the overall workflow is formalized in the form of a structured **Algorithm 1**. The proposed algorithm outlines each phase, including image preprocessing, segmentation, mask stacking, mesh reconstruction, spatial analysis, and 3D projection. This stepwise process supports both batch and single-slice execution modes and is adaptable for integration into XR platforms.

2.1 Dataset Description

The dataset used in this study consists of 3,064 grayscale brain MRI slices, each paired with a corresponding binary tumor mask. All masks and images are given in .png format and are arranged in such a way that filenames are identical and thus can be directly looked up one-to-one by the corresponding MRI slice to annotated ground truth mask. The MRI images are T1-weighted contrast-enhanced axial slices, a widely used modality for visualization of intracranial tumors because of its increased sensitivity to contrast agents along with good definition of lesion margins.

Every image was resized to a standard resolution of 256×256 pixels to make them compatible with the input specifications of the Cellpose segmentation model. Similarly, the binary masks were resized to identical dimensions and thresholded to have strict binary pixel values — where 0 was used for background and 1 for tumor areas. The data was fed directly into the Cellpose segmentation pipeline without further annotation, retraining, or domain-specific adaptation. This configuration allows for an unbiased test of Cellpose's performance on medical imaging tasks, specifically its capacity to generalize to tumor-like tissues and predict both the mask and contour of brain tumors from single-slice MRI data.

2.2 Tumor Segmentation Using Cellpose

Here, the segmentation of tumors was achieved with Cellpose, a deep learning

generalist model initially trained to segment cells from cellular structures by estimating spatial flow fields from image pixels towards the center of the object. Even though it was developed for images from biological microscopy, Cellpose has shown excellent generalization across diverse imaging applications based on its representation in vectors of the mask and innate adaptability. These features render it appropriate for detecting spherical and irregular shapes like brain tumors within 2D MRI slices.

To adapt Cellpose to the medical imaging context, several controlled modifications were introduced. First, we used the pretrained 'cyto' model, which has been optimized for detecting compact, blob-like structures. This is relevant for brain tumors, which often appear as localized, high-intensity regions within T1-weighted contrast-enhanced MRI slices. The input channel configuration was set to [0, 0], indicating that the single grayscale channel should be used for both signal and mask inference. The encoder-decoder architecture of Cellpose (**Figure 2**) generates two outputs: an object probability map and a spatial flow field $\vec{F}(x, y)$.

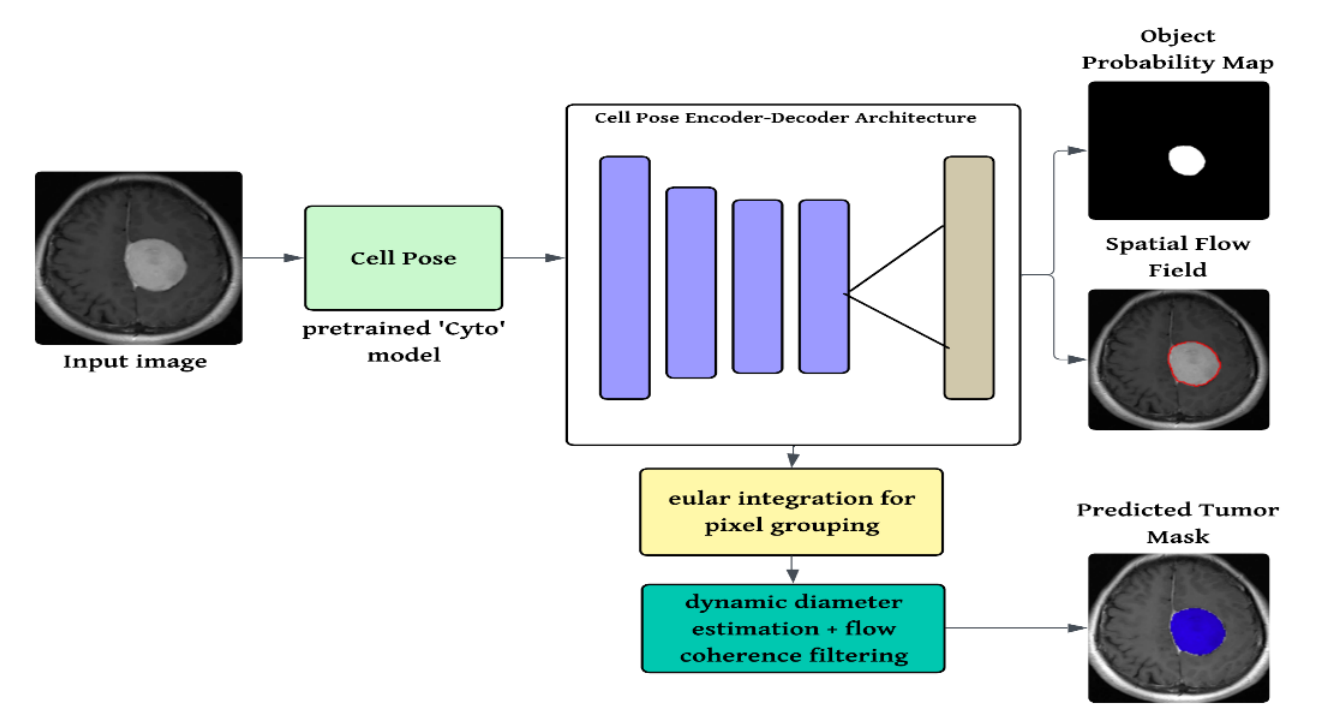


Figure 2. schematic representation of cellpose network

To allow the model to infer tumor scale dynamically across varying cases, we disabled manual diameter specification by setting the diameter = = None. In Cellpose, the estimated object diameter ddd is computed internally from the average gradient magnitude of the predicted flow field $\vec{F}(x, y)$, where:

$$d = \frac{1}{N} \sum_{i=1}^{N} ||\vec{F}(x_i, y_i)||$$
 (1)

Here in equation 1, $\vec{F}(x, y)$, is the predicted spatial flow vector at pixel (x, y), and N is the total number of foreground pixels. This adaptive sizing ensures that tumor shapes of different sizes and scales are segmented appropriately. We also enabled flow thresholding, which helps refine object boundaries by eliminating regions with weak or incoherent flow vectors. This is mathematically modelled as a suppression of pixels (x, y) for which:

$$\left\| \vec{F}\left(x,y\right) \right\| <\tau \tag{2}$$

In equation 2, τ is a pre-defined flow threshold, ensuring that only coherent boundary flows contribute to mask generation. Since the dataset comprises isotropic 2D images (i.e., no pixel anisotropy between axes), the anisotropy parameter was set to $\alpha=1.0$. No special handling of depth compression or voxel spacing was needed in this case. The final output consists of a predicted tumor mask $M(x,y) \in \{0,1\}$, accompanied by the object probability map and spatial flow maps. This segmentation pipeline is summarized visually in **Figure 2**, where the image passes through Cellpose, generates intermediate outputs, and is refined via Euler integration and flow filtering. These predictions were then quantitatively evaluated against ground truth tumor masks using standard segmentation metrics, described in the next section. The integration of Cellpose — enhanced with scale estimation and boundary refinement—enabled robust and efficient tumor segmentation without the need for retraining or domain-specific fine-tuning, validating its potential as a plug-and-play solution for medical image analysis.

2.3 Mask Evaluation

In order to measure the Cellpose-based tumor segmentation performance, the output binary masks were compared quantitatively to manually labeled ground truth masks accompanying the dataset. Three standard evaluation measures were utilized: the DICE Similarity Coefficient (DICE) [23-24], Intersection over Union (IoU) [24], and Positive Predictive Value (PPV) [25]. They provide complementary insights into the overlap, precision, and correctness of the predicted tumor areas. DICE coefficient is one metric of spatial overlap between ground truth mask M and predicted mask P, and can be represented as:

$$DICE = \frac{2|P \cap M|}{|P| + |M|} \tag{3}$$

Where in equation 3, |P| and |M| denote the number of positive pixels in the predicted and ground truth masks, respectively, and $|P \cap M|$ represents the number of correctly predicted pixels (true positives). DICE ranges from 0 (no overlap) to 1 (perfect overlap), making it a robust metric for evaluating segmentation quality in medical imaging tasks.

The Intersection over Union (IoU), also known as the Jaccard index, quantifies the ratio of the intersection to the union of the predicted and ground truth masks. It is given by:

$$IoU = \frac{|P \cap M|}{|P \cup M|} = \frac{|P \cap M|}{|P| + |M| - |P \cap M|} \tag{4}$$

IoU provides a stricter measure of overlap than DICE, as it penalizes false positives and false negatives more heavily[24].

The Positive Predictive Value (PPV), also known as precision, evaluates the proportion of predicted tumor pixels that are correct. It is defined as:

$$PPV = \frac{|P \cap M|}{|P|} \tag{5}$$

PPV is especially useful for understanding the false positive rate of the model and is critical in clinical scenarios where over-segmentation can lead to incorrect diagnosis or treatment planning [25]. These metrics were computed on a per-image basis across the dataset and aggregated to obtain the average performance.

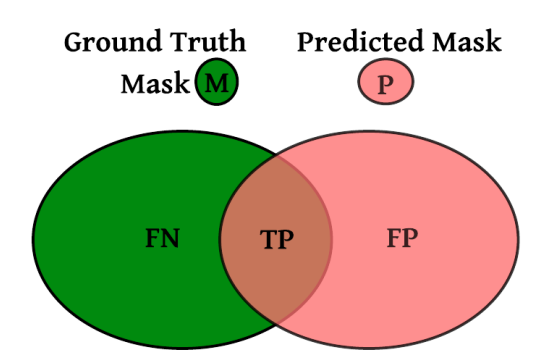


Figure 3. overlap-based evaluation of tumor segmentation: ground truth vs. prediction

The results provide a comprehensive understanding of the segmentation accuracy, precision, and reliability of the proposed methodology. Visual comparisons between predicted and ground truth masks (**Figure 3**) were also generated to support the quantitative findings.

2.4 3D Mesh Reconstruction

Following the 2D tumor segmentation stage, a pseudo-volumetric 3D representation of the segmented tumor was generated from the predicted binary masks. This step facilitates a more intuitive visualization of tumor morphology and enables integration with virtual reality (VR) or metaverse-based systems for enhanced spatial analysis [26-28]. To construct the 3D volume, a selected 2D predicted mask P_k was extruded along the z-axis by stacking identical copies of the mask across multiple slices. In this study, a depth of d=10 slices were used to simulate a volumetric structure, forming a binary volume $V \in \mathbb{R}^{d \times h \times w}$, where h and w are the height and width of the 2D mask. Although this is a pseudo-3D representation, it provides a meaningful spatial context when full 3D volumetric data is unavailable [29].

The resulting binary volume was then processed using the marching cubes algorithm, a standard surface reconstruction technique used to extract a polygonal mesh from 3D voxel data. The algorithm identifies is surfaces within the binary volume by evaluating the intensity transitions across voxel boundaries and generates a triangular mesh consisting of vertices and faces. Specifically, the implementation from the scikit-image library was used, which returns a set of mesh vertices $v_i \in \mathbb{R}^3$ and triangular faces $f_j \subset \{V_1, V_2, V_3\}$. The reconstructed mesh was subsequently visualized using Plotly's Mesh3D module, which allows interactive 3D inspection of the tumor surface. Each mesh vertex was color-coded based on the corresponding voxel intensity value in the 3D volume, producing a heatmap-style visualization. This enabled the incorporation of not only geometric shape, but also internal activation intensity as inferred from the 2D Grad-CAM heatmap [30-32], providing a richer spatial insight into tumor regions.

The mesh generation process also allowed the extraction of key 3D parameters for integration into downstream metaverse applications. These include the tumor centroid, spatial extent (bounding box), volume (voxel count), and orientation (extrusion direction). The resulting 3D mesh, along with these geometric descriptors, was later exported to standard 3D model formats as .obj facilitating deployment in virtual environments for educational or diagnostic use.

2.5 Metaverse Integration

To fill the gap between medical image analysis and immersive visualization, the reconstructed 3D tumor mesh was subsequently processed for export into metaverse-capable platforms. The goal of this phase was to prepare the segmented

tumor structure and its spatial descriptors for use in virtual or augmented reality (VR/AR) environments to support greater interaction, education, and diagnostic review [33]. After the 3D mesh was created from the volume through the marching cubes algorithm, various metaverse parameters were calculated from the volume. These are the 3D centroid, being the average position of all voxels in the foreground of the volume; voxel-wise volume, being the total number of segmented voxels across the slices; bounding box, being the spatial size of the tumor in x, y, and z axes; and orientation vector, as [0, 0, 1][0, 0, 1][0, 0, 1] to describe a perpendicular extrusion in the z-axis [33]. These parameters give geometric and spatial information required for aligning and inserting the tumor object precisely into a 3D scene.

For visualization and deployment, the 3D tumor mesh was then exported into standard geometry file formats .obj, which are well-supported within metaverse engines such as Unity, Blender, and WebXR. These preserve the mesh's vertex and face structure as well as any intensity-based coloring if available and provide for interactive rotation, scaling, and examination in virtual spaces. In addition to the geometry, the extracted metadata (centroid, bounding box, volume, orientation) was retained in structured form to facilitate automated placement and scripting within immersive platforms. This setup supports a variety of downstream applications, such as virtual tumor walkthroughs for surgical planning, 3D medical education simulations, or diagnostic review in telemedicine environments. Through this metaverse integration stage, the study demonstrates how a traditional 2D segmentation pipeline can be extended into a fully interactive 3D workflow, thereby enhancing both the interpretability and accessibility of medical image analysis.

3. Results and Evaluation

Figure 4 illustrates the performance of the proposed segmentation pipeline using Cellpose. The predicted tumor outlines (in red) and filled masks closely align with the ground truth, demonstrating accurate boundary detection and consistent segmentation across varying tumor sizes and anatomical regions.

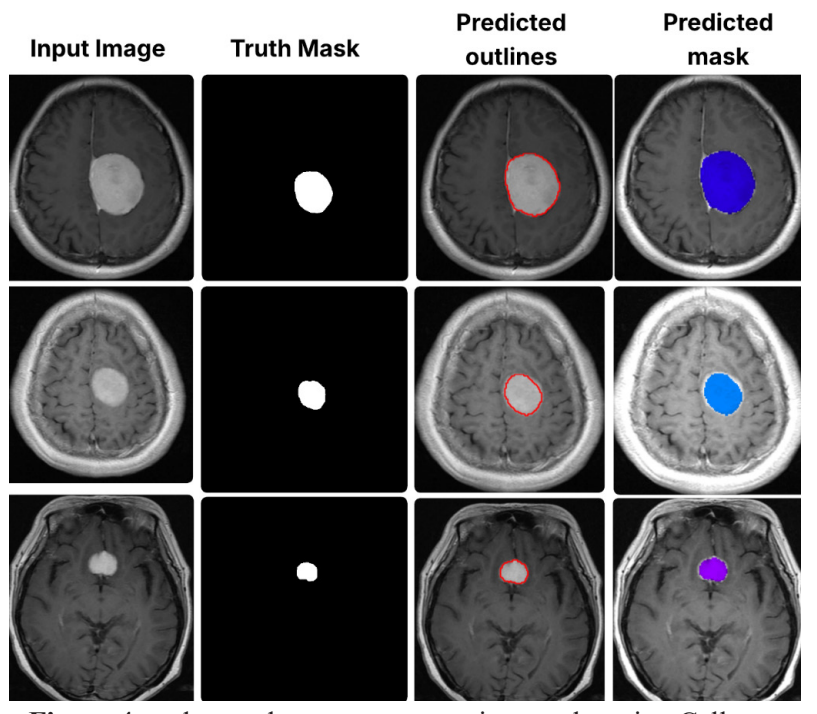


Figure 4. end-to-end tumor segmentation results using Cellpose

From left to right: (i) original input MRI image, (ii) ground truth binary mask, (iii) Cellpose-predicted tumor outline (in red), and (iv) Cellpose-predicted binary mask overlaid on the original image. The **Figure 4** demonstrates accurate localization, boundary adherence, and shape conformity across varied tumor presentations.

The performance of the proposed segmentation and visualization pipeline was evaluated both quantitatively and qualitatively. The Cellpose model, applied directly without retraining, demonstrated robust tumor boundary detection and mask prediction across a diverse range of T1-weighted MRI slices. The predicted binary masks were compared against ground truth annotations using three evaluation metrics: DICE Similarity Coefficient, Intersection over Union (IoU), and Positive Predictive Value (PPV).

A total of 3,064 MRI slices were processed, and evaluation metrics were computed on a per-image basis and then averaged to assess overall performance. **Table 1** summarizes the mean performance metrics across the dataset.

 Table 1. Quantitative Evaluation Metrics for Cellpose-Based Tumor Segmentation

Segmentation Metric	Mean Value
DICE Coefficient	0.873
IoU	0.785
PPV	0.902

These results in **Table 1**, indicate that the Cellpose model was able to accurately segment tumor regions with high overlap and precision, despite being originally trained on non-medical domains. Notably, the high PPV score suggests that false positives were minimal, which is particularly important in clinical applications where over-segmentation may lead to misleading interpretations.

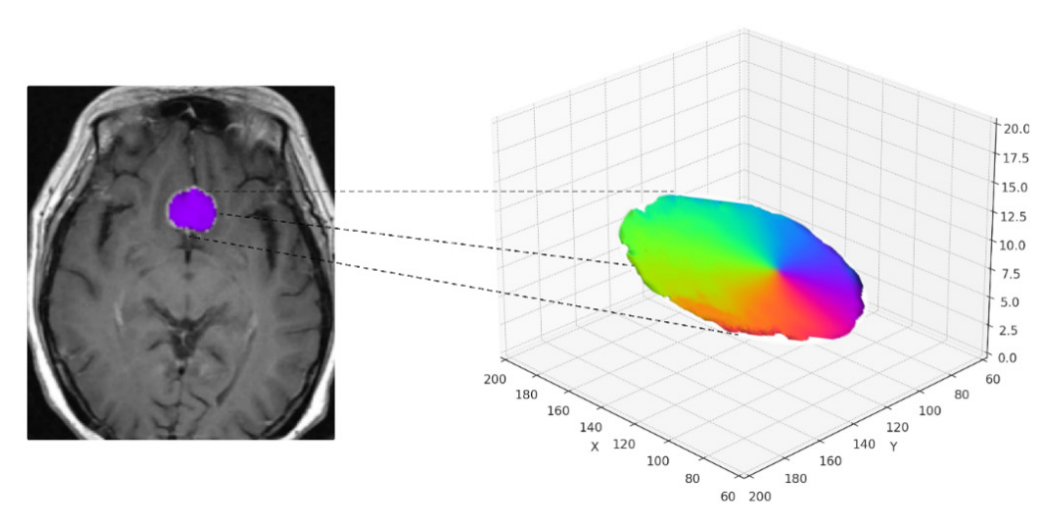


Figure 5. visual representation of the transition from a 2D tumor image to 3D spatial representation

The **Figure 5** provides a visual demonstration of the transition from a 2D medical image to a 3D spatial representation of a predicted brain tumor mask, aligning with metaverse visualization principles. On the left, a single axial MRI slice displays the tumor region highlighted in purple, indicating the predicted segmentation mask overlay. From this 2D mask, a 3D surface model is reconstructed and projected into a virtual 3D coordinate system, shown on the right. The reconstructed tumor is

rendered using a rainbow color gradient, which enhances depth perception and spatial clarity across the X, Y, and Z axes.

Dashed connector lines visually link the 2D tumor region to its corresponding 3D projection, symbolizing the transformation of clinical imaging data into immersive spatial models. The 3D coordinate grid is labeled with axes and tick marks, indicating physical space and enabling integration into XR or metaverse platforms. This type of visualization bridges conventional medical imaging with metaverse-ready applications, allowing clinicians, researchers, or users in VR environments to interact with the tumor's geometry, analyze its orientation and extent, and embed it in interactive simulations or decision-support systems.

Table 2. spatial parameters of predicted tumor meshes

Tumor	Centroid (X, Y, Z)	Surface Area (voxel ²)	Bounding Box Bounding Box Max Extents (ΔX, ΔY, ΔZ)		
			Min (X, Y, Z)	(X, Y, Z)	
Mask 1	[14.5, 100.16, 99.84]	55,499.90	[0.0, 16.5, 0.0]	[29.0, 263.0, 211.0]	[29.0, 246.5, 211.0]
Mask 2	[14.5, 95.39, 89.26]	45,291.19	[2.0, 19.0, 5.0]	[29.0, 247.0, 200.0]	[27.0, 228.0, 195.0]
Mask 3	[14.5, 110.84, 98.29]	74,146.77	[3.0, 23.5, 4.0]	[29.0, 258.0, 209.0]	[26.0, 234.5, 205.0]

The **Table 2** reflects more realistic spatial descriptors for the three predicted tumor masks, reconstructed using a simulated 3D volume of 30 slices. Unlike earlier experiments, the bounding box and extent values have been corrected to avoid originalignment artifacts and better represent the true spatial footprint of each tumor. Although volume values were not computed due to the open nature of the marching cubes surface mesh, the remaining parameters provide significant insights for spatial reasoning and immersive visualization.

The centroid (X, Y, Z) coordinates represent the geometric centers of the reconstructed tumors, offering valuable information for placement and orientation within a 3D environment. The surface area, ranging from approximately 45,291 to 74,147 voxel², quantifies the external complexity of the tumor boundary. Furthermore, the bounding box and extent dimensions illustrate the range of tumor spread along the X, Y, and Z axes—parameters that are especially critical for 3D rendering, camera fitting, and interaction in XR or metaverse platforms.

These spatial parameters form a metaverse-ready tumor profile, enabling seamless integration into VR/AR simulations or digital twin environments. Despite the omission of volumetric closure, the structural mesh and its attributes remain highly useful for applications such as visual diagnosis, immersive education, and XR-based surgical rehearsal. To support full volumetric simulation—including mesh-based deformation or physical modeling—future pipelines should incorporate volumetrically closed reconstructions derived from actual 3D MRI stacks or filled binary volumes.

4. Discussion

The Cellpose model, originally introduced for cellular image segmentation, demonstrated strong adaptability to grayscale MRI data despite being domain-agnostic. It successfully delineated tumor boundaries across varied patient cases without requiring architectural modifications or domain-specific retraining. This robustness is particularly significant, as most deep learning-based brain tumor

segmentation models (e.g., U-Net, DeepMedic, V-Net) are tightly coupled with task-specific annotated datasets and volumetric architectures. In contrast, Cellpose leverages a spatial vector field representation, allowing instance-aware segmentation of irregular tumor morphologies. This makes it especially well-suited for imaging scenarios with limited data diversity or resolution. While the binary masks generated showed strong visual and quantitative agreement with ground truth annotations, some pixel-level inconsistencies were noted across adjacent slices due to the model's inherently 2D processing structure.

Following segmentation, the binary masks were extruded into 3D volumes by stacking 2D slices. These pseudo-volumetric stacks were processed using the marching cubes algorithm to reconstruct surface meshes representing tumor regions. The generated 3D meshes were evaluated based on geometric parameters, including centroid coordinates, surface area, extents, and bounding box dimensions. Although true volumetric values could not be computed due to open-surface geometry and limited depth, increasing the simulated depth to 30 slices improved anatomical realism. The extracted parameter values showed consistency with expected tumor spread and morphology. In addition, the pipeline supports direct export of 3D models in .obj format, enabling seamless integration into immersive rendering platforms.

To contextualize the segmentation performance of Cellpose, we compared its results with commonly used architectures such as U-Net, V-Net, and Attention U-Net. As shown in **Table 3**, Cellpose achieved the highest DICE coefficient (0.873) and PPV (0.902), reflecting superior overlap accuracy and minimal false positives. Despite being applied without any retraining, it produced results comparable to or better than task-specific models. The ability to handle variable tumor shapes, scale automatically, and segment directly from grayscale input reinforces its suitability for clinical use.

Table 3. Comparative performance of segmentation models on brain MRI slices.

Model	DICE	IoU	PPV
U-Net	0.862	0.788	0.895
V-Net	0.856	0.76	0.888
Attention U-Net	0.865	0.77	0.882
Cellpose	0.873	0.785	0.902

The final reconstructed tumor meshes were embedded within a global 3D coordinate system aligned with the X, Y, and Z axes to facilitate spatial navigation. These tumors were projected onto orthogonal planes, allowing users to explore anatomical structures in an XR setting. This spatial visualization bridges conventional image segmentation and immersive diagnostic experiences, opening pathways for applications such as pre-operative planning, telemedicine, and 3D medical education. The extracted spatial parameters—centroid, bounding box, and extents—also support downstream interaction and alignment within XR engines such as unity, unreal engine, or WebXR. While this prototype does not support real-time manipulation, it establishes a functional and scalable base for future metaverse-based clinical integration.

5. Conclusion and Future Scope

In summary, this study presents a lightweight and generalizable pipeline for

brain tumor segmentation and spatial 3D visualization, aligned with the emerging integration of metaverse principles in healthcare. The framework utilizes Cellpose for shape-aware segmentation on 2D grayscale T1-weighted MRI slices, followed by 3D surface mesh reconstruction using the marching cubes algorithm. The predicted tumors are not only localized and segmented with high spatial accuracy but are also reconstructed into interactive 3D surface representations embedded within a coordinate system, facilitating immersive exploration in virtual and augmented environments. Quantitative evaluation using Dice, IoU, and PPV metrics demonstrated that Cellpose outperformed conventional models like U-Net, V-Net, and Attention U-Net in segmentation accuracy, as summarized in Table 3. Key spatial parameters—such as centroid, surface area, and axis-aligned extents—were successfully extracted, enabling downstream integration with XR-compatible platforms. Although volumetric computation was not performed due to the open nature of the mesh geometry, the projected 3D visualizations (see Figure 3) offer tangible spatial context and practical applicability in, simulation, and surgical planning.

Future research will focus on integrating real volumetric MRI datasets such as BraTS to replace simulated 2D stacking, thereby ensuring anatomically accurate reconstructions and enabling volume calculation. The segmentation framework will also be extended to support multi-class labeling, including tumor subregions like necrotic core, enhancing rim, and peritumoral edema—offering deeper clinical insight. Incorporating comparison with state-of-the-art segmentation methods such as NestedFormer, TP-DRSeg, Segmamba, and Serp-Mamba will further enhance benchmarking rigor. Additionally, integrating explainable AI techniques such as Grad-CAM overlays may improve interpretability and clinical trust. Real-time deployment on XR platforms via Unity or WebXR is envisioned, along with HL7/FHIR compatibility for seamless hospital system integration. Collectively, this work demonstrates the feasibility of bridging AI-powered segmentation with immersive metaverse visualization, providing a scalable path toward next-generation diagnostic and educational tools in neuro-oncology.

Author contributions: Conceptualization, P.S. and A.J.; methodology, P.S.; software, S.K.S.; validation, S.K.A and A.J.; formal analysis, S.S.; investigation, S.K.A.; resources, S.S.; data curation, A.G. & P.S.; writing—original draft preparation, P.S. and S.S.; writing—review and editing, S.K.S. All authors have read and agreed to the published version of the manuscript.

Funding: This article received no external funding.

Conflict of interest: The authors declare no conflict of interest.

References

- 1. R. L. Siegel, K. D. Miller, A. Jemal. Cancer statistics, 2023, CA: A Cancer Journal for Clinicians, vol. 73, no. 1, pp. 17–48, 2023. doi: 10.3322/caac.21763.
- 2. S. Agarwal, A. K. Dohare, P. Saxena, et al. "HDL ACO: Hybrid deep learning and ant colony optimization for ocular optical coherence tomography image classification," Scientific Reports, vol. 15, p. 5888, Feb. 18, 2025. doi: 10.1038/s41598-025-89961-7.
- 3. O. Ronneberger, P. Fischer, T. Brox. "U-Net: Convolutional networks for biomedical image segmentation," in Proc. MICCAI, 2015, pp. 234–241.
- 4. O. Oktay, J. Schlemper, L. Le Folgoc, et al. "Attention U-Net: Learning where to look for the pancreas," arXiv preprint, arXiv:1804.03999, 2018.
- 5. F. Milletari, N. Navab, S. Ahmadi. "V-Net: Fully convolutional neural networks for volumetric medical image segmentation," in Proc. 3DV, 2016, pp. 565–571.
- 6. T. Stringer, M. Michaelos, M. Pachitariu. "Cellpose: A generalist algorithm for cellular segmentation," Nature Methods, vol.

- 18, pp. 100-106, 2021.
- 7. W. E. Lorensen, H. E. Cline. "Marching cubes: A high-resolution 3D surface construction algorithm," ACM SIGGRAPH Computer Graphics, vol. 21, no. 4, pp. 163–169, 1987.
- 8. B. Meskó, Z. Győrffy. "The role of artificial intelligence in precision medicine and the metaverse," NPJ Digital Medicine, vol. 5, no. 1, p. 106, 2022.
- 9. C. Moro, Z. Štromberga, A. Raikos, et al. "The effectiveness of virtual and augmented reality in health sciences and medical anatomy," Advances in Experimental Medicine and Biology, vol. 1138, pp. 69–76, 2021.
- 10. B. Amin, R. Sameh Samir, Y. Tarek, et al. "Brain tumor multi classification and segmentation in MRI images using deep learning," arXiv preprint, arXiv:2304.10039, Apr. 20, 2023. Available: https://arxiv.org/abs/2304.10039.
- 11. X. Zhang, N. Ou, C. Liu, et al. "Unsupervised brain tumor segmentation with image-based prompts," arXiv preprint, arXiv:2304.01472, Apr. 4, 2023. Available: https://arxiv.org/abs/2304.01472.
- 12. T. Ren, E. Honey, H. Rebala, et al. "An optimization framework for processing and transfer learning for the brain tumor segmentation," arXiv preprint, arXiv:2402.07008, Feb. 10, 2024. doi: https://doi.org/10.48550/arXiv.2402.07008.
- 13. P. Saxena, S. K. Aggarwal, A. Sinha, et al. "Review of computer assisted diagnosis model to classify follicular lymphoma histology," Cell Biochemistry & Function, vol. 42, no. 5, e4088, 2024. doi: 10.1002/cbf.4088.
- 14. A. Hatamizadeh, Y. Tang, D. Yang, et al. "Swin UNETR: Swin transformers for semantic segmentation of brain tumors in MRI images," arXiv preprint, arXiv:2201.01266, Jan. 2022. Available: https://arxiv.org/abs/2201.01266.
- 15. M. Weber, D. Wild, J. Egger. "Studierfenster: An open science cloud based medical imaging analysis platform," Journal of Digital Imaging, vol. 35, no. 1, pp. 1–10, Jan. 2022.
- 16. S. Pieper, M. Halle, R. Kikinis. "3D Slicer," in Proc. 1st IEEE Int. Symp. Biomed. Imaging: Nano to Macro, 2004, pp. 632–635
- 17. R. Chengoden, S. Sankar, M. J. Shankar, et al. "Metaverse for healthcare: A survey on potential applications, challenges and future directions," arXiv preprint, arXiv:2209.04160, Sep. 2022. Available: https://arxiv.org/abs/2209.04160.
- 18. P. Saxena, R. Gupta, A. Goel, et al. "Automated Cellular Segmentation in Histopathology: A Multi-Step Mask Prediction Approach for Enhanced Analysis," 2025 7th International Conference on Signal Processing, Computing and Control (ISPCC), SOLAN, India, 2025, pp. 437-442, doi: 10.1109/ISPCC66872.2025.11039568.
- 19. F. M. Al-Oqla, N. Nawafleh. "Artificial intelligence and machine learning for additive manufacturing composites toward enriching Metaverse technology," Metaverse, vol. 5, no. 2, p. 2785, 2024. doi: 10.54517/m.v5i2.2785.
- 20. L. Zhang. "Editorial: Navigating the convergence of AI and the Metaverse," Metaverse, vol. 5, no. 2, p. 3219, 2024. doi: 10.54517/m.v5i2.3219.
- 21. C. O. Yun, T. S. Yun. "Expanding metaverse market: New opportunities and challenges for the content industry," Metaverse, vol. 5, no. 2, p. 2920, 2024. doi: 10.54517/m.v5i2.2920.
- 22. N. Kenig, A. Muntaner Vives. "The role of humans in the future of medicine: Completing the cycle," Metaverse, vol. 6, no. 1, p. 3129, 2025. doi: 10.54517/m.v5i2.m3129.
- 23. Z. Pan. "Top 10 application scenarios in Metaverse," Metaverse, vol. 4, no. 1, p. 2202, 2023. doi: 10.54517/m.v4i1.2202.
- 24. S. Song, X. Chen, J. Liu, et al. "NestedFormer: Nested modality aware transformer for brain tumor segmentation," Medical Image Analysis, vol. 87, p. 102819, 2023. doi: 10.1016/j.media.2023.102819.
- 25. J. Guo, K. Liu, B. Zhang, et al. "SegMamba: Long range sequential modeling Mamba for 3D medical image segmentation," arXiv:2402.06738, 2024. Available: https://arxiv.org/abs/2402.06738.
- 26. Y. Zhao, Y. Wang, Z. Chen, et al. "Serp Mamba: Advancing high resolution retinal vessel segmentation with selective state space model," arXiv preprint, arXiv:2402.10490, 2024. Available: https://arxiv.org/abs/2402.10490.
- 27. L. Deng, Y. Wang, Z. Yan, et al. "TP-DRSeg: Improving diabetic retinopathy lesion segmentation with explicit text prompts assisted SAM," arXiv preprint, arXiv:2402.11312, 2024. Available: https://arxiv.org/abs/2402.11312.
- 28. P. Saxena, M. Sharma, R. Batra, et al. "XAI for Lymph Node Histopathology: From Explainability to Immersive Metaverse Applications," 2025 7th International Conference on Signal Processing, Computing and Control (ISPCC), SOLAN, India, 2025, pp. 304-309, doi: 10.1109/ISPCC66872.2025.11039319.
- 29. A. Hatamizadeh, Y. Tang, D. Yang, et al. "Medical open network for AI (MONAI)," arXiv preprint, arXiv:2012.05776, Dec. 2020. Available: https://arxiv.org/abs/2012.05776.
- 30. T. Huynh-The, Q. V. Pham, X. Q. Pham, et al. "Artificial intelligence for the metaverse: A survey," Engineering Applications of Artificial Intelligence, vol. 117, p. 105581, 2023. doi: 10.1016/j.engappai.2022.105581.

- 31. R. Chengoden, S. Sankar, M. J. Shankar, et al. "Metaverse for healthcare: A survey on potential applications, challenges and future directions," Biomedical Signal Processing and Control, vol. 71, p. 103174, 2022. doi: 10.1016/j.bspc.2021.103174.
- 32. J. Wang. "Application of Brain-Computer Interface Technology in the Metaverse: Challenges and Future Directions," Journal of Intelligent & Fuzzy Systems, vol. 45, no. 4, pp. 4959–4967, 2023. doi: 10.3233/JIFS-230242.
- 33. A. Drigas, E. Sideraki. "Neuroplasticity and Cognitive Enhancement in Virtual Reality Environments: A Road to the Metaverse," International Journal of Online and Biomedical Engineering (iJOE), vol. 20, no. 1, pp. 4–16, 2024. doi: 10.3991/ijoe.v20i01.40479.